POLITECNICO DI TORINO
Repository ISTITUZIONALE

Optimization of Laser-Induced Graphene Electrodes for High Voltage and Highly Stable Microsupercapacitors

Original
Optimization of Laser-Induced Graphene Electrodes for High Voltage and Highly Stable Microsupercapacitors / Zaccagnini, P., Tien, Y., Baudino, L., Pedico, A., Bianco, S., Lamberti, A.. - In: ADVANCED MATERIALS TECHNOLOGIES. - ISSN 2365-709X. - (2023), pp. 1-10. [10.1002/admt.202300833]

Availability:
This version is available at: 11583/2983649 since: 2023-11-07T14:36:36Z

Publisher:
Wiley

Published
DOI:10.1002/admt.202300833

Terms of use:

This article is made available under terms and conditions as specified in the corresponding bibliographic description in the repository

Publisher copyright

(Article begins on next page)

13 September 2026

Check for updates

ADVANCED MATERIALS TECHNOLOGIES
www.advmattechnol.de

Optimization of Laser-Induced Graphene Electrodes for High Voltage and Highly Stable Microsupercapacitors

Pietro Zaccagnini, Ye Tien, Luisa Baudino, Alessandro Pedico, Stefano Bianco, and Andrea Lamberti*

Microsupercapacitors (μSCs) have received a lot of interest for their possible use in miniaturized electronics and in the field of the Internet of Things (IoT) to power distributed sensors. μSCs fill the gap between batteries and traditional capacitors, providing high power densities and acceptable energy densities to fulfill onboard power supply requirements, coupled with quick charge/discharge rates and extended lifetime. Charge balancing of μSCs is not a standard practice, although the optimization of electrodes can provide beneficial effects on the electrochemical performance and stability of the device. In this work, a charge-balanced double-layer μSC based on laser-induced graphene (LIG) with [PYR14][TFSI] as an ionic liquid electrolyte is presented for the first time. The optimized device shows an improvement in terms of the increased lifetime of a factor of four and its energy efficiency is raised above 80%.

1. Introduction

The miniaturization of electronic devices is the future and current trend. The Internet of Things (IoT) and the smartphone markets are driving this trend, for instance, from handled devices to medical applications.[1–5] Further, the request for miniaturized electronic devices and components able to operate in harsh environmental conditions such as high temperatures, mechanical vibrations, and in the presence of chemicals is constantly increasing.[6–8] Printed circuit boards (PCBs) are getting miniaturized since passive components are moving towards the 01005-packaging Surface Mount Devices (SMD) standard, and passive components are the ones occupying the larger percentage of the PCB itself. Some actual PCBs like the Arduino Nano RP2040 are equipped with 0201 SMD and several functional integrated circuits (ICs). In some cases, energy storage devices (ESD) such as batteries and supercapacitors (SCs) are required to be on the PCB for functional reasons such as autonomous operation in those places where power supply cannot directly be provided. In these situations, batteries play a major role because of their higher energy density per square centimeter but SCs are helpful whenever the battery module cannot be oversized to guarantee power densities, or in less energetic demand-like situations. This is the case of another commercial solution on the Portenta Machine Control PCB from Arduino. This IoT board is equipped with a commercial SC of about 0.5 cm^3 and a volumetric density of about 0.2 F cm^{-3}. Miniaturized SCs are referred to as micro-SCs (μSCs), especially those obtained via IC-like manufacturing technology. μSCs can buffer high power requirements from the electronics and in some cases, like in automotive or servers, they can buffer power run-out letting the electronics perform backup operations in a few minutes. In these scenarios, the main power supply is not located on the PCB but is centralized and distributes energy to on-site electronics. Furthermore, distributed sensor networks[9,10] which might not be easily accessible for maintenance might require integrated energy harvesting and storage solutions to provide the needed energy.[11] For these reasons, optimized ESDs are required to carry on these jobs in the most efficient way. ESD electrodes are balanced to maximize their energy content by exploiting the maximum voltage at maximum charge storage capabilities since energy is proportional to the product QV for both batteries and SCs.

SCs are divided into electrical double-layer capacitors (EDLCs) and pseudocapacitors. EDLCs store charge in an electrostatic process while pseudocapacitors store energy thanks to fast and energetically distributed redox reactions resulting in an overall device response closer to a capacitive system. Battery-like materials with outstanding power capabilities enter the SC area but the response is non-capacitive meaning that the V versus Q characteristic is nonlinear. Electrodes with different storage mechanisms can be combined in asymmetric devices. Electrodes with the same storage mechanism can instead be combined in a symmetrical configuration. However, to exploit the maximum voltage, electrode charges must be balanced to avoid polarization issues, regardless of the device architecture. In this work, an EDLC μSC will be

P. Zaccagnini, Y. Tien, L. Baudino, A. Pedico, S. Bianco, A. Lamberti
Department of Applied Science and Technologies - Polytechnic of Turin
Corso Duca degli Abruzzi 24, Torino 10129, Italy
E-mail: pietro.zaccagnini@polito.it
P. Zaccagnini, A. Pedico, A. Lamberti
Centre for Sustainable and Future Technologies - Italian Institute of Technologies
Via Livorno 60, Torino 10144, Italy

The ORCID identification number(s) for the author(s) of this article can be found under https://doi.org/10.1002/admt.202300833

© 2023 The Authors. Advanced Materials Technologies published by Wiley-VCH GmbH. This is an open access article under the terms of the Creative Commons Attribution-NonCommercial License, which permits use, distribution and reproduction in any medium, provided the original work is properly cited and is not used for commercial purposes.

DOI: 10.1002/admt.202300833

studied and optimized hence, from now on, the discussion will be related to these types of devices.

The balance of the charges is of paramount importance, and in EDLC the need for it mainly comes from the tradeoff between the ions' charge densities/mobilities and the electrochemical stability of the electrolyte at the interfaces.[12,13] Electrodes will show different capacitances and potential limits in anodic and cathodic polarization, but since the overall charge must be the same within the maximum voltage window,

$$\begin{aligned} Q_+ &= Q_- \\ CV|_+ &= CV|_- \end{aligned} \tag{1}$$

In the case of μSC, capacitances are evaluated per cm^2 and are called areal capacitances. By making the quotient between the areal charges, the ratio between the area of the electrodes to get a balanced device is defined. This problem is often, but not always, faced in the design phase of a supercapacitor and allows the maximization of the coulombic efficiency within the maximum voltage window, the stability of the device, and the energy efficiency. This practice is not always implemented in the case of planar SC and is mostly neglected in the case of μSC. Only one very recent paper discusses this issue among thousands of works in literature.[14] μSCs differ from the macroscopic devices firstly for the miniaturization as well as for the configuration of the electrodes, which can be interdigitated or even thread-like in the so-called wire-shaped devices. Within μSC technology, also the so-called parallel configuration is aimed to maximize the areal quantities, as discussed in the literature.[15–17]

Herein, we first report the charge balance of laser-induced graphene (LIG)-based μSC in ionic liquid (IL) electrolyte. LIG carbon-based materials are obtained via photothermal conversion of polymers under laser radiation. The laser conversion process has been well-known since the middle of the '900, but the material was proven to be graphene-like only in 2014.[18–21]

LIG is widely used in μSC technology due to its simplicity of production and the possibilities stemming from its substrate flexibility.[22–25] Furthermore, LIG represents an excellent starting point for the subsequent device optimization with pseudocapacitive and EDLC materials deposition on the 3D carbon network or surface functionalization treatments, that significantly increase their energy storage performance.[26–28]

Laser writing simplifies the tuning of the electrical and electrochemical properties of the resulting graphene by acting on the laser parameters like power, frequency, and scanning velocity. When the best writing parameters are defined, they are used to laser-write both electrodes of the μSC. For this reason, one method to balance the charges is to work directly on the μSC design in terms of area ratio. In this work, we present the results of the optimization of the device geometry to get a balanced μSC in IL electrolytes. For the first time, we also present a three-electrode characterization setup exploiting the LIG itself as a pseudo-reference material in the electrolytic environment. Carbon materials are known to be exploitable as pseudo-reference systems.[29] Because of its relatively high surface area, LIG can be assumed to be non-polarizable in the working electrode (WE)–reference electrode (REF) potential probes mesh in the potentiostat, unless adsorption phenomena occur as described by Ruch et al.[29]

The devices were optimized to work with the IL electrolyte [PYR14][TFSI]. The charge balancing optimization was performed by evaluating specific areal capacities and unbalancing the interdigitated electrodes areas. According to our measurements, the final device voltage is 3.0 V with electrodes area ratio of 1.4 and a specific areal capacitance of 1.3 mF cm^{-2} rated at 10 μA cm^{-2}. The energy performances were 1.4 μWh cm^{-2} at 6.7 μW cm^{-2} and 0.8 μWh cm^{-2} at 130 μW cm^{-2}. The device could deliver more than roughly 60% of its energy/capacity at relatively high current rate of 200 μA cm^{-2}. Finally, with respect to a nonoptimized device, its lifetime was increased by four times, according to our floating tests results.

2. Results and Discussions

The analysis started with the investigation of the material square resistance variations due to the velocity sweep scan. Interdigitated electrodes for electrochemical design procedures and Van der Pauw geometries were printed without the support of hard masks, and these geometries are reported in **Figure 1**. Figure 1a shows the geometries printed without hard masks, while Figure 1b depicts the mask-assisted printing procedure highlighting that in this case the laser is not employed to mark selectively a particular feature, but it is raster scanned over a surface inscribing the geometry to be printed.

The produced geometries via hard mask-assisted printing were investigated through electron microscopy. As reported in Figure 1c–e, mask assisted LIG printed features show a systematic deviation of 20–30 μm on the lateral dimension with respect to the mask nominal width. On the other hand, features obtained by constraining the geometry by means of a computer aided design (CAD) input showed larger deviations with respect to the nominal feature size due to the laser spot size, which is 370 μm in diameter at full power in our setup. The laser spot size, related to the printed LIG feature, was demonstrated to be power dependent at fixed scan speed.[30] Such dependency justifies the possibility to get features as wide as 130 μm, approximatively, on a CAD geometry of nominal 100 μm. However, the relative error is larger for non-masked processes and lower for masked ones as reported in **Table 1**. As can be evinced from Figure 1c–h, the relative error of masked assisted LIG prints is below 25%. For these reasons we decided to exploit a masking solution to better control the printed geometries ensuring a precise control of the area ratio. In Figure S1 (Supporting Information) we report the printing result of a 270 μm printed LIG digit. Concerning the morphological aspects, both masked and non-masked samples show macroporosities with average diameter below 10 μm. However, the mask-assisted printed samples show uniform and not

Table 1. Relative errors of printed geometries with respect to physically imposed feature dimension (masked process) and CAD driven laser scribing procedures (non-masked).

Feature size [μm]	Masked [%]	Non-masked [%]
100	23.3	31.1
150	20.5	77.5
200	10.8	50.5

© 2023 The Authors. Advanced Materials Technologies published by Wiley-VCH GmbH

2365709x, 0, Downloaded from https://onlinelibrary.wiley.com/doi/10.1002/admt.202300833 by Politecnico Di Torino Sist. Bibl Del Polit Di Torino, Wiley Online Library on [07/11/2023]. See the Terms and Conditions (https://onlinelibrary.wiley.com/terms-and-conditions) on Wiley Online Library for rules of use; OA articles are governed by the applicable Creative Commons License

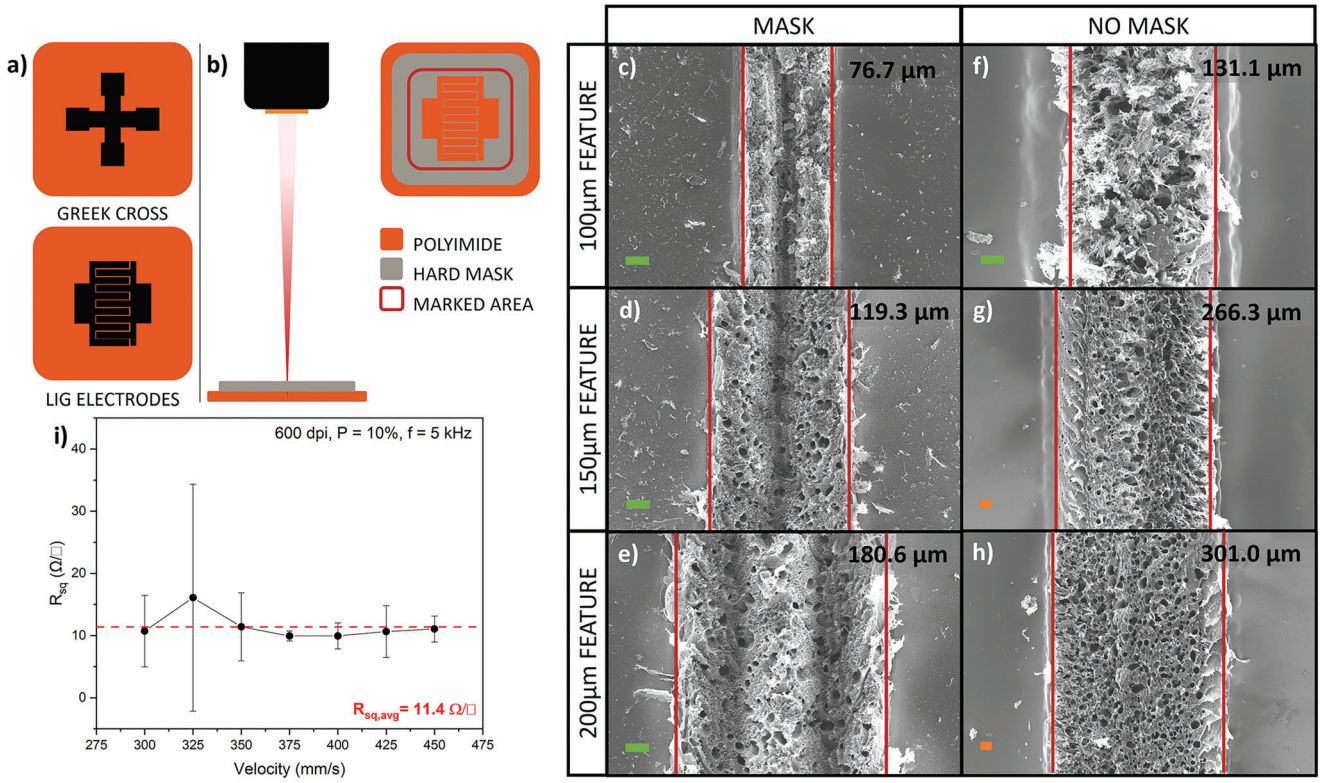

Figure 1. a) The Greek cross printed without the hard mask support and the LIG interdigitated electrodes. b) A scheme of the hard mask-assisted printing method. Panels c-h) report the FESEM images derived for features with lower dimension in the range [100, 200] μm, the colored bar indicates a 20 μm unit. In particular, c–e) show the results for mask-assisted LIG printed features, while f–h) the ones obtained by constraining the geometry with the laser software. i) Square resistance at different raster scan velocities, with fixed filling density, power, and frequency.

rough evolution even for smaller features (Figure 1c compared to 1f), probably due to the writing method causing less heat concentration in the laser scribed area. Interestingly, masked samples show a possible nonuniform in plane LIG distribution due to single slit diffraction effects, as might happen in lithographic processes.

The conductivity of the different samples was indirectly measured using the Van der Pauw method on LIG Greek crosses. Several combinations of parameters were tested starting from the information obtained from a previous work concerning frequency, laser power, and writing velocity.[31] Five crosses per parameter set were printed to get average information about the sheet resistance. The interesting result was that the electrical properties of the produced LIG were independent of the raster scan velocity at fixed power of 10%, frequency of 5 kHz, and density of 600 dpi, as reported in Figure 1i. The result can be due to the density of points per unit distance, imposing low displacements such that the overall scan velocity was reduced and slightly affected by the velocity parameter. The average square resistance measured for the set of parameters 600 dpi, 10% power, 5 kHz, and different velocities was 11.4 Ω $\square^{-1}$. This result is shown in Figure 1d. For this reason, the set of parameters 600 dpi, 10% power, 5 kHz, and 375 mm s^{-1} was chosen to print geometries for the electrochemical characterizations. The sheet resistance values obtained for different sets of parameters are reported in Figure 1d. Although the slightly lower values of resistances, the material produced with such geometries turned out to be fragile and not processable.

In general, it was observed that while decreasing raster speed and frequency, i.e., increasing fluence, the square resistance decreases at fixed power and dpi. Also, LIG produced under these high fluence conditions results in being mechanically unstable, hence the measured sheet resistance value is altered by material loss because of ablation. The density of pulses also affects LIG production. In fact, at fixed power and frequency, low densities such as 100 dpi and 200 dpi are not enough to ensure PI conversion. This proves that the overall fluence can be controlled by increasing the density of laser spot shots, by causing overlapping of laser spots. According to the work of Ming et al., the sheet resistance of LIG is not only dependent on the produced material density but also on the overall thickness of the produced material.[32]

2.1. Charge Balancing

Electrochemical cells for half-cell measurements and device measurements were assembled according to the scheme reported in **Figure 2**. Further details are reported in Figure S2 (Supporting Information).

To carry on charge balancing of the interdigitated electrodes, half-cell measurements were performed to characterize the anodic and cathodic properties of LIG with [PYR14][TFSI] IL. CV measurements were run at 5 mV s^{-1}, at increasing polarization potential of the electrodes with a step of 100 mV. Coulombic efficiency was evaluated cycle by cycle to determine anode and

© 2023 The Authors. Advanced Materials Technologies published by Wiley-VCH GmbH

2365709x, 0, Downloaded from https://onlinelibrary.wiley.com/doi/10.1002/admt.202300833 by Politecnico Di Torino Sist. Bibl Del Polit Di Torino, Wiley Online Library on [07/11/2023]. See the Terms and Conditions (https://onlinelibrary.wiley.com/terms-and-conditions) on Wiley Online Library for rules of use; OA articles are governed by the applicable Creative Commons License

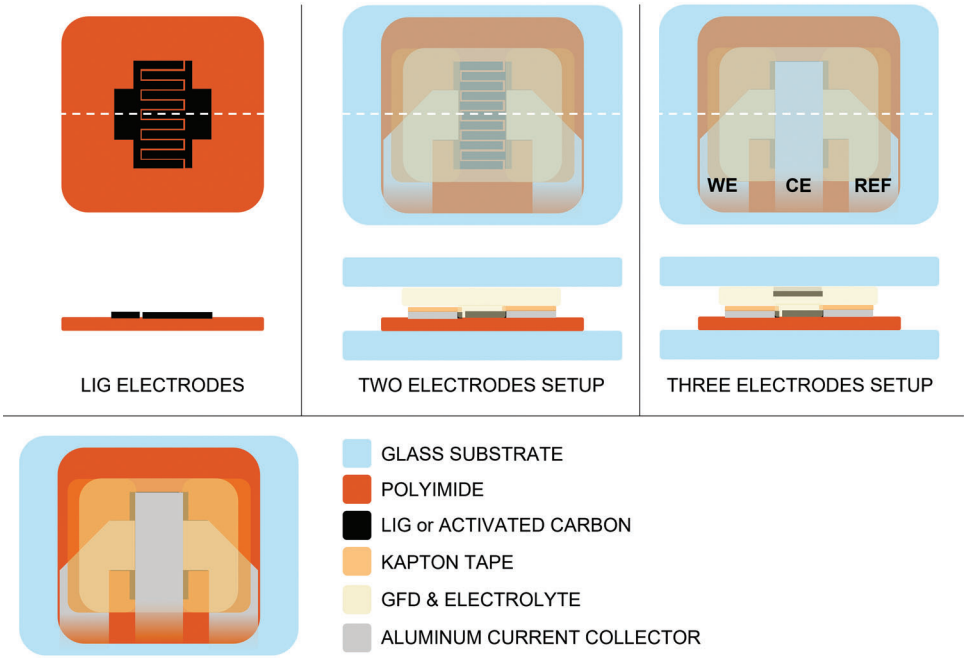

Figure 2. Printed LIG electrodes. Electrochemical cell architectures for the device and the three electrodes setups.

cathode working over-potentials. The results are depicted in **Figure 3**. As shown in panel a), an efficiency threshold of 99.0% was set. However, we noticed a systematic trend of coulombic efficiencies in cathodic polarization lower than the threshold value. This was attributed to oxygen contamination. Although the cells were vacuum sealed, one cannot exclude the possibility that in the dry room environment, some oxygen contaminations could be present dissolved in the electrolyte and as small residuals in the pouch cell after the sealing process, thus leading to oxygen reduction reactions (ORR). Literature reports confirmed this hypothesis since in the work of Monaco et al. ORR was characterized in O_2 saturated [PYR14][TFSI] and a quasi-reversible process was observed in the bare electrolyte.[33] Additionally to the quasi-reversible process, it is not excluded that the slightly inefficient cathodic behavior can be ascribed to the superoxide radical anion, $O_2^{\cdot-}$, side reactions with the IL itself, as shown by the work of Schwenke et al.[34] Moreover, it is well known in the literature that surface properties of carbons influences the ORR process.[35] The surface of carbons is often full of oxygen-based functional groups and all of them are considered as mediators in the ORR reaction.[35–38] According to our Raman spectra results reported in Figure 3c, the produced LIG is oxidized as the spectrum is much closer to graphene oxide and carbon blacks.[39] According to the Raman measurements results, the average I_D/I_G and I_{2D}/I_G were 0.48 and 0.39, respectively, akin to a highly defective multilayer graphene structure.[40] The HWHM (half width half maximum) were evaluated by roughly fitting the peaks with one Lorentzian function each, around the peak center. Their values suggest the presence of oxidized species, as well as the presence of a shoulder above the G mode. Further details are provided in Tables S3 and S4 (Supporting Information). Independently from the peaks ratios, we noticed in all the ten acquired spectra a tiny peak at 2320 cm^{-1} with low intensity, which can be attributed to the presence of C—N, C═N or C≡N groups.[41] In a previous work,[31] this Raman evidence was not highlighted; however, although small, the presence of nitrogen groups was also proved through XPS analyses, where the presence of C—N bonds could be seen in the HR spectra of both C1s (at ≈286 eV) and N1s (at 400.3 eV) regions.[42,43] From the XPS survey, reported in Figure S3 (Supporting Information), the nitrogen presence is shown. Further, in Table S5 (Supporting Information), the nitrogen presence is evidenced to be 1.5 at% from quantitative HR analyses. The XPS deconvolution of the C1s and N1s is further reported in Figure S4 (Supporting Information). Both oxygen and nitrogen groups are able to interact with hydrophobic ionic liquids, such as [PYR14][TFSI], repulsively due to Van der Waals interactions, hence reducing the surface wettability.[44,45] Moreover, nitrogen groups have been shown to improve ORR activity even at low concentration levels.[46] Since, as reported in Table S5 (Supporting Information), the overall amounts are low (1.5 at% for N1s and 5.4 at% for O1s), the material can be considered suitable for the application. The small atomic percentage concentration of nitrogen in the LIG also explains the low intensity peak in the Raman spectra associated to nitrogen groups.

Assuming the EDL charging-discharging process of the cation of high coulombic efficiency, we selected the polarization level of −1.8 V as the polarization limit in the presence of concurrent OR as reported in Figure 3b. The result is in good agreement with the literature, as reported in the work of Pohlmann.[12] After this electrode polarization level all the parallel electrochemical processes, that is, ORR and IL cation reduction and irreversible reactions contribute to the decrease in the coulombic efficiency. Regarding the anodic polarization limit, the coulombic efficiency exhibited a decline below 99.0% when exceeding 1.2 V. Hence, this specific polarization level was selected for the subsequent calculations. The determination of specific capacities involved analyzing the

© 2023 The Authors. Advanced Materials Technologies published by Wiley-VCH GmbH

2365709x, 0, Downloaded from https://onlinelibrary.wiley.com/doi/10.1002/admt.202300833 by Politecnico Di Torino Sist. Bibl Del Polit Di Torino, Wiley Online Library on [07/11/2023]. See the Terms and Conditions (https://onlinelibrary.wiley.com/terms-and-conditions) on Wiley Online Library for rules of use; OA articles are governed by the applicable Creative Commons License

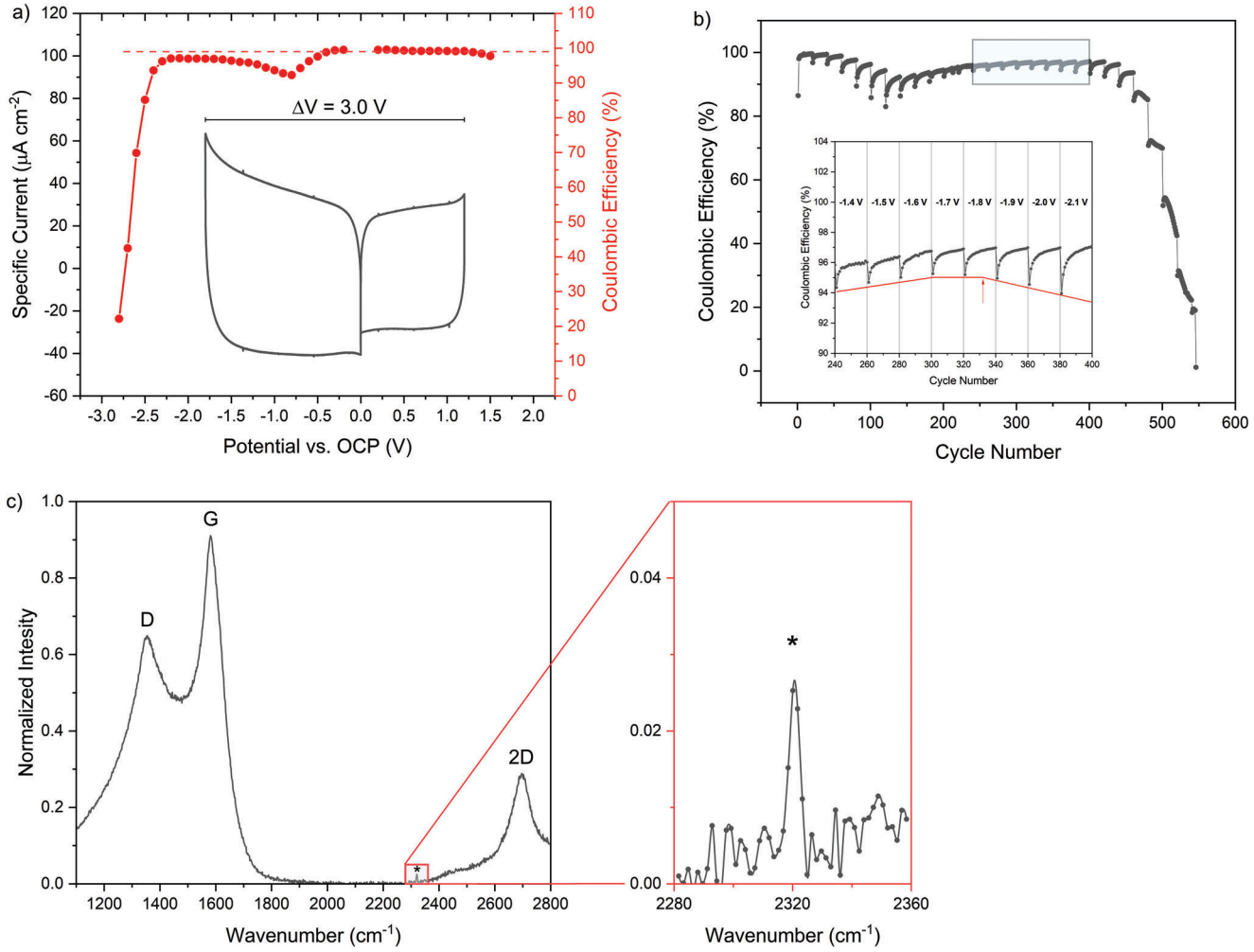

Figure 3. a) The results of the anodic and cathodic measurements performed at 5 mV s^{-1}. b) An explicit view of the used criterion to select the cathodic polarization limit. c) The recorded Raman spectrum of the produced LIG.

discharge profiles at the defined anodic and cathodic polarization limits. These values were employed to derive the optimized area ratio between the positive and negative electrodes. Consequently, the resulting area ratio for the optimized device was determined to be $r = A_+/A_- = 1.4$.

2.2. Device Characterization

Preliminary CV and EIS tests were run on different areal-balanced devices to prove the early effectiveness of the optimization procedure. The tested devices were differing in the areal ratio between the electrodes, the values being: 1.0, 1.4, and 1.6. The device with an area ratio of 1.6 was studied to get redundant information to the non-optimized symmetric device. The optimized device was the one with an electrode area ratio of 1.4. EIS was run to evaluate eventual strong differences in the tested μSCs. CVs were run at 10 mV s^{-1} for 100 cycles to observe the μSCs stability in the optimized voltage window of 3.0 V. The results are shown in **Figure 4**. In panel a) it is possible to observe that the symmetrical device clearly shows currents due to degradation processes. However, the effectiveness of the optimization procedure is better appreciated in Figure 4b where it is evident that the voltammogram closer to the ideal shape of an EDLC is the CV of the optimized device with an area ratio $r = 1.4$. In Figure 4c, capacitance retentions and coulombic efficiencies are reported to better appreciate the advantages of μSCs optimization. The coulombic efficiency was greater than 98.0% only for the optimized device while for the not optimized devices the coulombic efficiency was below 95.0%. Concerning capacitance retention, performances were close for devices with ratios of 1.4 and 1.6, while the symmetrical device suffered the biggest loss in the early stages of the CV experiment. The Nyquist plots of Figure 4d show the cells impedances prior to the CV measurements. Especially for the 1.0 and 1.6 cells, the open circuit EIS spectra are similar. The optimized cell shows a slightly increased resistive behavior. This can be due to the initial wettability of the sample since, while cycling the cell, similar resistive properties of the non-optimized cells can be observed from the CV plots in Figure 4b. Hence, the cells can be considered comparable from the cell impedance point of view. Moreover, the evolution of the imaginary parts of the three devices represents the correct behavior since the capacitance trend

© 2023 The Authors. Advanced Materials Technologies published by Wiley-VCH GmbH

2365709x, 0, Downloaded from https://onlinelibrary.wiley.com/doi/10.1002/admt.202300833 by Politecnico Di Torino Sist. Bibl Del Polit Di Torino, Wiley Online Library on [07/11/2023]. See the Terms and Conditions (https://onlinelibrary.wiley.com/terms-and-conditions) on Wiley Online Library for rules of use; OA articles are governed by the applicable Creative Commons License

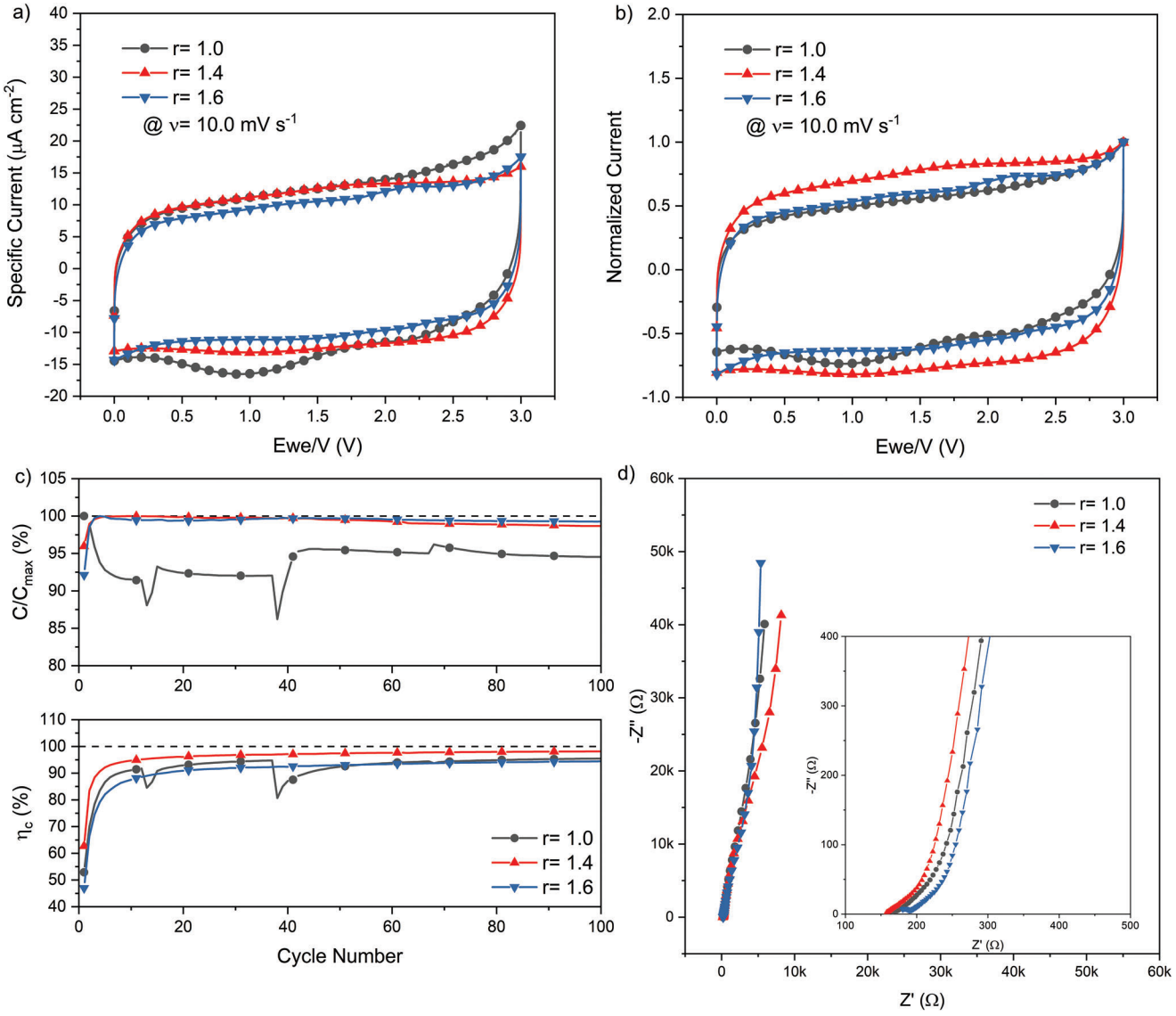

Figure 4. a) 100th CV cycles recorded at 10 mV s^{-1} in the optimized window for ratios of 1.0, 1.4 (optimized), and 1.6. b) Normalized currents of the voltammograms recorded in a) to show that the optimized device shows the most ideal EDLC box shape. c) Capacitance retentions and coulombic efficiencies of the CV tests. d) The Nyquist plots of the different cells show similar resistive properties.

reflects the order 1.0, 1.4, and 1.6. These claims were further proved by fitting the impedance spectra by means of a slight deviation of the equivalent circuit proposed by Dsoke et al.[47] In that circuit, a series between a Warburg diffusion element in series with a capacitance (sometimes changed with a constant phase element, CPE) value is used to describe the middle to low frequency range. In our analyses, we condensed these two elements in the anomalous diffusion one provided in the EC-Lab software of BioLogic. Anomalous diffusion modeling was shown for both blocking and non-blocking interfaces.[48–50] The results of our fitting analyses are reported in Table S3 (Supporting Information). The main finding is related to the fact that most of the real part of devices impedance constituting the internal resistance of the device comes from the non-uniform microstructured LIG electrodes network.

Rate capability tests were run in galvanostatic mode on the optimized device. GCD was run at several current rates spanning in the range {10, 20, 50, 100, 200} μA cm^{-2}. The results are reported in **Figure 5**. In Figure 5a, the capacitance retention is reported versus the number of cycles at the different current rates for the tested devices. The not optimized devices retain less initial capacitance with respect to the optimized case. After the high-power tests, the optimized device recovers its initial capacitance. Further, at high current densities the device retains more than 60% of its initial capacitance. Remarkably, as shown in Figure 5b, the coulombic efficiency is close to 100% at all the GCD rates. In the not optimized cases the coulombic efficiency is lower at low current densities due to possible enhanced degradation phenomena. Accordingly, energy efficiency is lower for the not optimized devices especially at low current rates. The energy efficiency of the

© 2023 The Authors. Advanced Materials Technologies published by Wiley-VCH GmbH

2365709x, 0, Downloaded from https://onlinelibrary.wiley.com/doi/10.1002/admt.202300833 by Politecnico Di Torino Sist. Bibl Del Polit Di Torino, Wiley Online Library on [07/11/2023]. See the Terms and Conditions (https://onlinelibrary.wiley.com/terms-and-conditions) on Wiley Online Library for rules of use; OA articles are governed by the applicable Creative Commons License

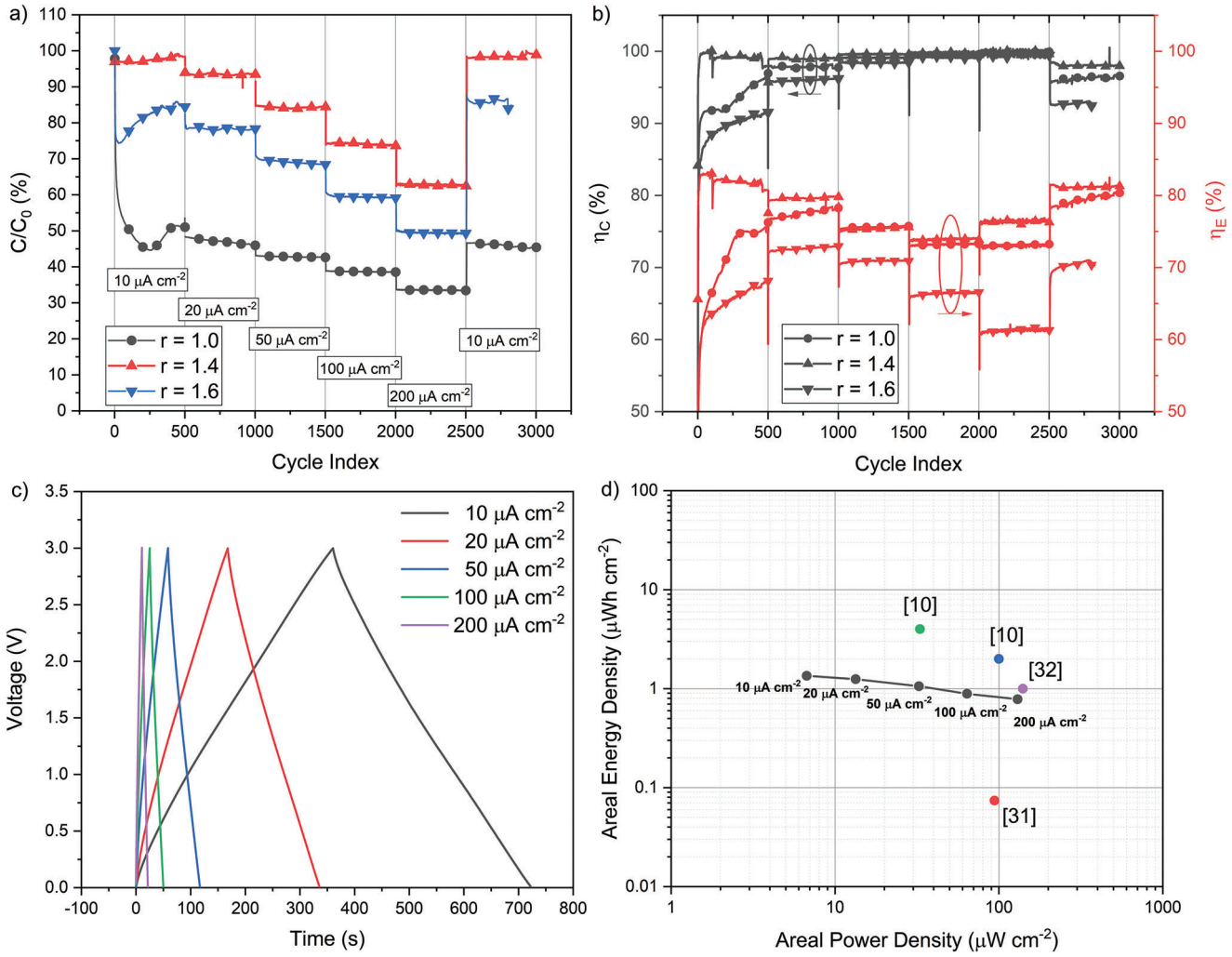

Figure 5. Optimized device electrochemical performance. a) The capacitance retention out of the rate capability test for the tested device of different area ratio. b) The corresponding coulombic and energy efficiencies versus cycle number. c) The galvanostatic profiles at the end of each current density test of the optimized device. d) The Ragone plot derived from the rate capability test of the optimized device.

optimized device, characterized by an area ratio of 1.4, demonstrates remarkable behavior. At a characteristic time of approximately 320 s (with a current density of 10 μA cm^{-2}), the energy efficiency reaches 81%. However, as the current density increases to 200 μA cm^{-2}, the efficiency decreases to around 70%, with the characteristic time reducing to approximately 10 s. These energy efficiency values are respectfully outperforming recent literature reports in which μSCs were reported with maximum 51.6% energy efficiency.[51] Indeed, as reported in Figure 5c, the ideal GCD profile is maintained during the current sweep and not much resistive contributions alters the device performance. Finally, the Ragone plot was evaluated out of this test, and it can be appreciated that the device operates at energy density levels of 1.0 μWh cm^{-2} and power densities of 0.1 mW cm^{-2}. These results are comparable with the literature reports although overwhelmed by pseudocapacitive devices especially in terms of energy densities.[14,16,21,52,53] The power capabilities are slightly limited by the resistive nature of the electrodes, and, partially, of the electrolyte.

Float tests were performed as accelerated aging tests. At this point, only the devices with ratios $r = 1.0$ and $r = 1.4$ were tested. The FT cycle was composed of 50 GCD repetitions at 10 μA cm^{-2} followed by 20 h of voltage retention at the rated voltage of 3.0 V. The test was repeated for at least 500 h. The results are shown in **Figure 6**. Interestingly, both devices required several floating cycles to get a maximum capacitance value. However, after reaching a maximum capacitance value, devices started aging with different loss ratios. In fact, the optimized device showed a capacitance reduction rate of −0.0025% which is four times lower than the one of the symmetrical device, as reported in Figure 6a. Another result worth mentioning is given by the constant positive difference among the results concerning device efficiencies. As can be observed from Figure 6b, either in terms of coulombic or energy efficiency, the optimized device is constantly outperforming the other, in spite of the slight deviation that can be seen. Such ageing was not observed during high power rate cycling stability tests as reported in Figure S5 (Supporting Information). This test was performed at 100 μA cm^{-2} and both devices showed constant

© 2023 The Authors. Advanced Materials Technologies published by Wiley-VCH GmbH

2365709x, 0, Downloaded from https://onlinelibrary.wiley.com/doi/10.1002/admt.202300833 by Politecnico Di Torino Sist. Bibl Del Polit Di Torino, Wiley Online Library on [07/11/2023]. See the Terms and Conditions (https://onlinelibrary.wiley.com/terms-and-conditions) on Wiley Online Library for rules of use; OA articles are governed by the applicable Creative Commons License

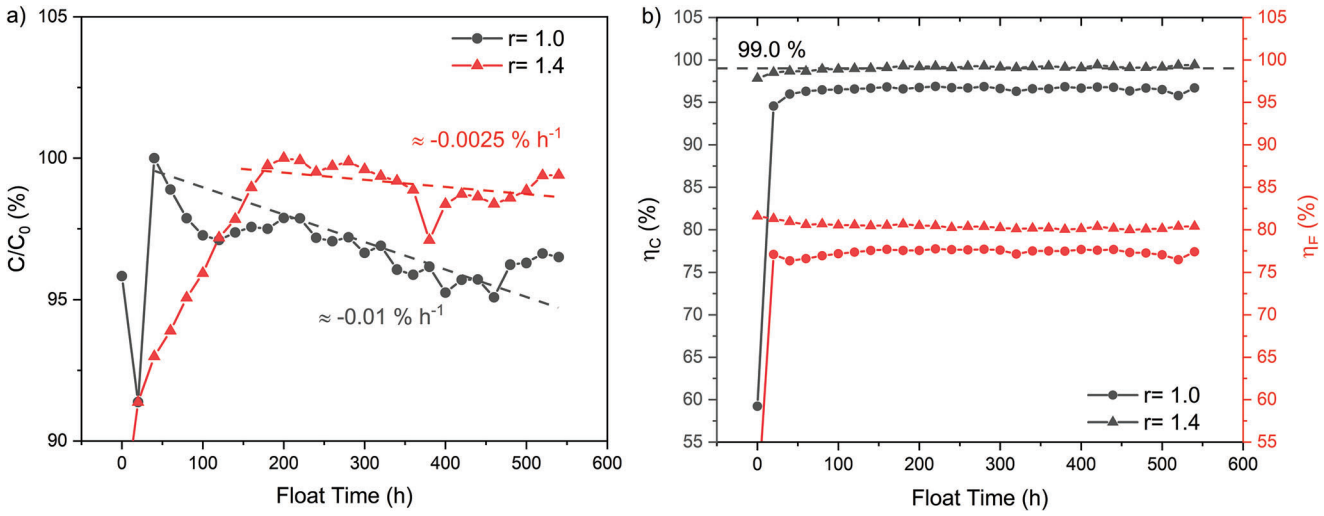

Figure 6. FT results differences between optimized and symmetrical devices reported versus the total floating time at rated voltage of 3 V. a) The capacitance retention shows a reduced aging time for the optimized device. b) The rated coulombic and energetic efficiencies of the two devices.

capacitance retention around 90%, although the not optimized device suffered from an initial loss. This result can be explained by considering that during cycling stability tests devices experience highly stressful conditions (high voltage) for a reduced amount of time with respect to the overall charge/discharge period. On the contrary, during floating tests, devices are subject to continuous stress condition. Such testing condition is closer to an application scenario in which SCs are constantly kept at full charge state to buffer eventual power supply runouts.

3. Conclusion

μSCs' charge balancing is not widely discussed in energy storage literature. This study focuses on designing a stable LIG μSC. A three-electrode setup was used to analyze the single electrode properties, and precise electrodes were fabricated using hard masks. Oxygen contamination's impact on performance was considered. Accelerated aging tests showed the engineered μSC had a four-fold longer lifetime than a non-optimized version. An optimized IL-based μSC at 3.0 V demonstrated average areal capacitance. Galvanostatic measurements at various currents revealed improved areal energy and power densities of 1.4 μWh cm^{-2} and 130.1 μW cm^{-2}, respectively. High energy efficiency (above 70%) was achieved at high current rates and above 80% at low rates. This optimization approach effectively prevents energy wastage and enhances device performance.

4. Experimental Section

Materials: Commercial Kapton tape of 125 μm thickness was used as process substrate. Samples were cleaned with ethanol prior to laser conversion. IL [PYR14][TFSI] was purchased by Solvionic with a purity of 99.9%. Since the assembly was carried out in dry room, the IL was stored under vacuum to avoid oxygen and atmospheric contaminations. Battery-grade aluminum purchased from S4R was used to contact LIG pads and to deposit activated carbon (AC) based slurries for the fabrication of the counter electrodes (CE). YP-50F AC was provided by Kuraray. C65 carbon black (CB) was provided by IMERYS. Sodium carboxymethylcellulose (CMC) was purchased by MTI. One gram of 85 wt% AC, 10 wt% CB, and 5 wt% CMC, was mixed in 5 mL of de-ionized water to produce a slurry. The slurry was deposited on the aluminum current collector through the doctor blade technique. Whatman glass fiber of grade D (GFD) was purchased by Sigma Aldrich. Aluminum laminated films for pouch cell casing were provided by Dai Nippon printing company, model D-EL408PH(3). Ethyl vinyl acetate (EVA) hot melt adhesive was used to guarantee the sealing of aluminum tabs to the pouch cell foils. EVA was provided by Shenzhen Tunsing Plastics Products Co., Ltd.

LIG Printing: LIG electrodes were fabricated with an EOX 30 W laser system provided by Datalogic. According to specifications, this laser system relies on the pulsed width modulation (PWM) control of the laser source. The PWM period is set through the frequency parameter and the duty cycle (DC) is set by the power parameter expressed as a percentage value. The laser spot for the selected focus (200 mm) is declared to be 370 μm.

Raman Analysis: Micro-Raman spectroscopy was performed by using a Renishaw InVia Qontor Raman microscope. A laser diode source (λ = 532 nm) was used with 5 mW power, and sample inspection occurred through a microscope objective (50×), with a backscattering light collection setup. The Raman spectra were acquired in the range [1100, 2800] cm^{-1}. Data analysis and baseline corrections were performed by means of Fityk software.

Hard Mask Preparation: Hard masks were prepared to assist the raster scan electrodes printing because of both hardware and software limitations of the CO_2 laser source. A stainless-steel foil of 100 μm thickness, provided by GoodFellow, was used to produce hard masks. An IR laser source (1064 nm) was used to pattern the electrodes of controlled ratios on the stainless steel; the spot size was 80 μm. The chosen set of parameters was 30 A current, 3 kHz frequency, 30 mm s^{-1} velocity, and the number of repetitions was set as high as to assure the proper drilling of the designed pattern, without any damage such as the bending of the foil. A table summarizing all the evaluated combinations is reported in Table S1 (Supporting Information). Devices were printed according to the scheme reproduced in Figure 1. The marked area was exposed to raster scan with the set of optimized parameters.

Sheet Resistance: Sheet resistance measurements were implemented to quantify the sheet resistance of the produced LIG. The measurements were carried out in a four-point probe setup with Keithley 2440A. Measurements were done at low currents avoiding the voltage to overcome a few millivolts.[54] The implemented geometry was the Greek cross, as reported in Figure 1. The square pad contacts were 1.4 × 1.4 mm in length, and the widths of the inner cross were 1.0 × 1.0 mm so the inner square resulted as 1.0 × 1.0 mm. The squared pads were covered by conductive silver paste,

© 2023 The Authors. Advanced Materials Technologies published by Wiley-VCH GmbH

2365709x, 0, Downloaded from https://onlinelibrary.wiley.com/doi/10.1002/admt.202300833 by Politecnico Di Torino Sist. Bibl Del Polit Di Torino, Wiley Online Library on [07/11/2023]. See the Terms and Conditions (https://onlinelibrary.wiley.com/terms-and-conditions) on Wiley Online Library for rules of use; OA articles are governed by the applicable Creative Commons License

contacts were made with spring probes to assure good pressure on the pads.

Electrochemical Measurements and Data Analysis: Electrochemical measurements were performed by means of a VMP3 workstation provided by BioLogic, controlled by means of EC-Lab software. Cyclic voltammetry (CV), galvanostatic charge and discharge (GCD) protocols, and electrochemical impedance spectroscopies (EIS) were run to completely characterize both the devices and the single electrodes. Potentiostatic experiments were run at a constant resolution of 100 µV. EIS probe signal was of 5 mV amplitude and frequencies were let sweep from 1 down to 10 MHz, 10 points per decade, averaging four periods per frequency. Float test (FT), cycling stability test (CS), and GCD experiments were implemented on Arbin BT2000. Arbin tests were run on both optimized and non-optimized devices. GCD experiments were run at different current densities of {10, 20, 50, 100, 200} µA cm^{-2}. FT was run with 50 cycles of GCD performed at 10 µA cm^{-2} followed by a constant voltage period of 20 h at rated voltage. The sequence was repeated for several days. CS was run at 100 µA cm^{-2} for 10 000 cycles to evaluate capacity retention upon cycling. Capacitances were derived from the energy, which was computed as

$$E = \int V(t)\, I(t)\, dt \tag{2}$$

and using

$$E = \frac{1}{2}\frac{Q^2}{C} \tag{3}$$

as known relations for the energy in capacitive systems relating the unknown capacitance and computable charge, according to

$$Q = \int I(t)\, dt \tag{4}$$

The power was calculated by applying

$$P = \frac{E}{\Delta t} \tag{5}$$

Charge balancing and device design can be carried out by means of three electrodes (half-cell) measurements. CVs were run in anodic and cathodic directions. LIG electrodes were initially stabilized in a symmetrical window of ±0.1 V versus OCP, 20 cycles, and then anodic and cathodic polarization steps were of 0.1 V in absolute value. Half-cell measurements were referred to a reference electrode (REF) potential of LIG in IL itself. The reliability of this pseudo-ref was indirectly derived by looking out for possible CE drifts during measurements. The main idea behind this choice was that the areal balancing of coplanar electrodes should be done with a coplanar reference system. Furthermore, since LIG has a relatively high surface, it must result non-polarizable in the WE-REF voltage probes mesh of the potentiostat. Hence, the half-cell test cell was composed of six and five interdigitated LIG electrodes, covered by GFD impregnated with IL. The area of a single digit in this architecture was 2.7 mm^2. The starting area ratio was 1.2. An AC-based electrode was placed in correspondence to the LIG interdigitated electrodes exposed to the electrolyte on top of the GFD. All three electrodes were probed by means of aluminum tabs. LIG electrodes were masked by Kapton tape to confine the electrolyte on the interdigitated area. WEs were always the six-digit side, REFs the five-digit ones. High surface area CEs were used to buffer the experiments' charge as much as possible to avoid decompositions at CE altering the chemistry of the cell. A scheme is depicted in Figure 2. Further details are provided in Figure S1 (Supporting Information).

Devices and half-cell cells were assembled in pouch cell packs. The LIG devices were held on a glass substrate and a glass substrate was used to uniformly compress the cell stacks under vacuum (more details are reported in the Supporting Information). Aluminum tabs were bonded to the pouch cell material under the hot press using EVA hot melt adhesive. The amount of electrolyte was 400 µL cm^{-2}. Assembled balanced devices were tested under CV at 10 mV s^{-1} in a rated voltage window and EIS to check transport properties. Galvanostatic charge-discharge (GCD) measurements at different current rates were performed to evaluate rate capabilities and build the Ragone plot. FTs were run to evaluate accelerated aging. A scheme for the device cell architecture is provided in Figure 2. Further details are provided in Figure S1 (Supporting Information). The device area was 0.5 cm^2.

Supporting Information

Supporting Information is available from the Wiley Online Library or from the author.

Acknowledgements

This result is part of a project that has received funding from the European Research Council (ERC) under the European Union's ERC Starting Grant agreement No. 949916. This study was carried out within the MOST – Sustainable Mobility Center and received funding from the European Union Next-Generation EU (PIANO NAZIONALE DI RIPRESA E RESILIENZA (PNRR) – MISSIONE 4 COMPONENTE 2, INVESTIMENTO 1.4 – D.D. 1033 17/06/2022,CN00000023). This manuscript reflects only the authors' views and opinions, neither the European Union nor the European Commission can be considered responsible for them.

Conflict of Interest

The authors declare no conflict of interest

Data Availability Statement

The data that support the findings of this study are available from the corresponding author upon reasonable request.

Keywords

charge balancing, energy efficiency, energy storage devices, ionic liquids, laser-induced graphene, supercapacitors

Received: May 23, 2023
Revised: August 9, 2023
Published online:

[1] L. Yin, J. Wang, *Natl. Sci. Rev.* **2022**, *10*, nwac060.
[2] J. Hyysalo, S. Dasanayake, J. Hannu, C. Schuss, M. Rajanen, T. Leppänen, D. Doermann, J. Sauvola, *Internet Things* **2022**, *18*, 100511.
[3] H. Pourrahmani, A. Yavarinasab, R. Zahedi, A. Gharehghani, M. H. Mohammadi, P. Bastani, J. Van Herle, *Internet Things* **2022**, *19*, 100579.
[4] L. Di, L. Vollero, M. Merone, *Internet Things* **2022**, *20*, 100614.
[5] U. Garlando, S. Calvo, S. Member, M. Barezzi, G. S. Member, A. Sanginario, *IEEE Trans. AgriFood Electron.* **2023**, 1, https://doi.org/10.1109/TAFE.2023.3284563.
[6] Z. Cao, Q. Wen, X. Wang, Q. Yang, F. Jiang, *J. Internet Things* **2021**, *3*, 11.
[7] G. Sinnapolu, S. Alawneh, *Internet Things* **2020**, *12*, 100277.
[8] S. Ai, A. Chakravorty, C. Rong, *Sensors* **2019**, *19*, 721.
[9] A. A. Helal, R. S. Villaça, C. A. S. Santos, R. Colistete, *Internet Things* **2022**, *19*, 100518.

© 2023 The Authors. Advanced Materials Technologies published by Wiley-VCH GmbH

2365709x, 0, Downloaded from https://onlinelibrary.wiley.com/doi/10.1002/admt.202300833 by Politecnico Di Torino Sist. Bibl Del Polit Di Torino, Wiley Online Library on [07/11/2023]. See the Terms and Conditions (https://onlinelibrary.wiley.com/terms-and-conditions) on Wiley Online Library for rules of use; OA articles are governed by the applicable Creative Commons License

[10] F. Ganz, D. Puschmann, P. Barnaghi, S. Member, F. Carrez, *IEEE Internet Things J.* **2015**, *2*, 340.
[11] R. Speranza, P. Zaccagnini, A. Sacco, A. Lamberti, *Sol. RRL* **2022**, *6*, 2200245.
[12] S. Pohlmann, R. S. Kühnel, T. A. Centeno, A. Balducci, *ChemElectroChem* **2014**, *1*, 1301.
[13] S. Pohlmann, C. Ramirez-Castro, A. Balducci, *J. Electrochem. Soc.* **2015**, *162*, A5020.
[14] B. Asbani, K. Robert, P. Roussel, T. Brousse, C. Lethien, *Energy Storage Mater.* **2021**, *37*, 207.
[15] N. A. Kyeremateng, T. Brousse, D. Pech, *Nat. Nanotechnol.* **2017**, *12*, 7.
[16] C. Lethien, J. Le Bideau, T. Brousse, *Energy Environ. Sci.* **2019**, *12*, 96.
[17] T. Guillemin, C. Douard, K. Robert, B. Asbani, C. Lethien, T. Brousse, J. Le Bideau, *Energy Storage Mater.* **2022**, *50*, 606.
[18] M. Schumann, R. Sauerbrey, M. C. Smayling, *Appl. Phys. Lett.* **1991**, *58*, 428.
[19] X. J. Gu, *Appl. Phys. Lett.* **1993**, *62*, 1568.
[20] N. Arnold, N. Bityurin, *Appl. Phys. A* **1999**, *68*, 615.
[21] J. Lin, Z. Peng, Y. Liu, F. Ruiz-Zepeda, R. Ye, E. L. G. Samuel, M. J. Yacaman, B. I. Yakobson, J. M. Tour, *Nat. Commun.* **2014**, *5*, 5714.
[22] A. Velasco, Y.u K. Ryu, A. Boscá, A. Ladrón-De-Guevara, E. Hunt, J. Zuo, J. Pedrós, F. Calle, J. Martinez, *Sustainable Energy Fuels* **2021**, *5*, 1235.
[23] J. M. Tour, Y. Li, R. Ye, Y. Chyan, C. J. Arnusch, S. P. Singh, *ACS Nano* **2018**, *12*, 2176.
[24] A. Lamberti, M. Serrapede, G. Ferraro, M. Fontana, F. Perrucci, S. Bianco, A. Chiolerio, S. Bocchini, *2D Mater.* **2017**, *4*, 035012.
[25] R. Ye, Y. Li, C. Kittrell, J. M. Tour, J. Zhang, X. Han, Y. Chyan, *Adv. Mater.* **2017**, *29*, 1702211.
[26] Y. Ji, L. Li, R. Ye, N. D. Kim, Y. Li, Y. Yang, H. Fei, G. Ruan, Q. Zhong, Z. Peng, J. M. Tour, J. Zhang, C. Gao, *Adv. Mater.* **2015**, *28*, 838.
[27] F. Clerici, M. Fontana, S. Bianco, M. Serrapede, F. Perrucci, S. Ferrero, E. Tresso, A. Lamberti, *ACS Appl. Mater. Interfaces* **2016**, *8*, 10459.
[28] M. Reina, A. Scalia, G. Auxilia, M. Fontana, F. Bella, S. Ferrero, A. Lamberti, *Adv. Sustainable Syst.* **2022**, *6*, 2100228.
[29] P. W. Ruch, D. Cericola, M. Hahn, R. Kötz, A. Wokaun, *J. Electroanal. Chem.* **2009**, *636*, 128.
[30] J. De La Roche, I. López-Cifuentes, A. Jaramillo-Botero, *Carbon Lett.* **2023**, *33*, 587.
[31] A. Lamberti, F. Perrucci, M. Caprioli, M. Serrapede, M. Fontana, S. Bianco, S. Ferrero, E. Tresso, *Nanotechnology* **2017**, *28*, 174002.
[32] M. Liu, J. N. Wu, H. Y. Cheng, *Sci. China Technol. Sci.* **2022**, *65*, 41.
[33] S. Monaco, A. M. Arangio, F. Soavi, M. Mastragostino, E. Paillard, S. Passerini, *Electrochim. Acta* **2012**, *83*, 94.
[34] K. U. Schwenke, J. Herranz, H. A. Gasteiger, M. Piana, *J. Electrochem. Soc.* **2015**, *162*, A905.
[35] B. Sljukic, C. E. Banks, R. G. Compton, *J. Iran. Chem. Soc.* **2005**, *2*, 1.
[36] M. S. Hossain, D. Tryk, E. Yeager, *Electrochim. Acta* **1989**, *34*, 1733.
[37] P. Chen, R. L. Mccreery, *Anal. Chem.* **1996**, *68*, 3958.
[38] T. Nagaoka, T. Sakai, K. Ogura, T. Yoshino, *Anal. Chem.* **1986**, *58*, 1953.
[39] L. Bokobza, J.-L. Bruneel, M. Couzi, *C* **2015**, *1*, 77.
[40] A. C. Ferrari, D. M. Basko, *Nat. Nanotechnol.* **2013**, *8*, 235.
[41] X. Wang, J. Wang, Z. Yang, Y. Leng, H. Sun, N. Huang, *Surf. Coat. Technol.* **2010**, *204*, 3047.
[42] J. Cai, C. Lv, A. Watanabe, *Nano Energy* **2016**, *30*, 790.
[43] D. W. Zeng, K. C. Yung, C. S. Xie, *Surf. Coat. Technol.* **2002**, *153*, 210.
[44] H. P. Boehm, *Carbon* **1994**, *32*, 759.
[45] M. Lazzari, M. Mastragostino, F. Soavi, *Electrochem. Commun.* **2007**, *9*, 1567.
[46] A. C. Ramírez-Pérez, J. Quílez-Bermejo, J. M. Sieben, E. Morallón, D. Cazorla-Amorós, *Electrocatalysis* **2018**, *9*, 697.
[47] S. Dsoke, X.u Tian, C. Täubert, S. Schlüter, M. Wohlfahrt-Mehrens, *J. Power Sources* **2013**, *238*, 422.
[48] J. R. Macdonald, L. R. Evangelista, E. K. Lenzi, G. Barbero, *J. Phys. Chem. C* **2011**, *115*, 7648.
[49] L. R. Evangelista, E. K. Lenzi, *Fractional Diffusion Equations and Anomalous Diffusion*, Cambridge University Press, Cambridge **2018**.
[50] P. Zaccagnini, L. Baudino, A. Lamberti, A. L. Alexe-Ionescu, G. Barbero, L. R. Evangelista, C. F. Pirri, *J. Electroanal. Chem.* **2022**, *918*, 116499.
[51] M. Gao, X. Dong, X. Mei, K. Wang, W. Wang, Z. Tang, W. Duan, *Chem. Eng. J.* **2023**, *471*, 144609.
[52] J. Xu, G. Shen, *Nano Energy* **2015**, *13*, 131.
[53] J. Lin, C. Zhang, Z. Yan, Y.u Zhu, Z. Peng, R. H. Hauge, D. Natelson, J. M. Tour, *Nano Lett.* **2013**, *13*, 72.
[54] D. K. Schroder, *Semiconductor Material and Device Characterization*, Wiley, New York **2006**.

© 2023 The Authors. Advanced Materials Technologies published by Wiley-VCH GmbH

2365709x, 0, Downloaded from https://onlinelibrary.wiley.com/doi/10.1002/admt.202300833 by Politecnico Di Torino Sist. Bibl Del Polit Di Torino, Wiley Online Library on [07/11/2023]. See the Terms and Conditions (https://onlinelibrary.wiley.com/terms-and-conditions) on Wiley Online Library for rules of use; OA articles are governed by the applicable Creative Commons License